

# Mapping optical scattering properties to physical particle information in singly and multiply scattering samples: supplement

**TAYLOR M. CANNON,<sup>1,2,\*</sup>  BRETT E. BOUMA,<sup>1,2</sup> AND NÉSTOR URIBE-PATARROYO<sup>2</sup> **

<sup>1</sup>*Massachusetts Institute of Technology, Institute of Medical Engineering and Science, 70 Massachusetts Avenue, Cambridge, MA 02141, USA*

<sup>2</sup>*Wellman Center for Photomedicine, Massachusetts General Hospital, 40 Blossom St, Boston, MA 02114, USA*

\*[cannonr@mit.edu](mailto:cannonr@mit.edu)

---

This supplement published with Optica Publishing Group on 27 July 2023 by The Authors under the terms of the [Creative Commons Attribution 4.0 License](#) in the format provided by the authors and unedited. Further distribution of this work must maintain attribution to the author(s) and the published article's title, journal citation, and DOI.

Supplement DOI: <https://doi.org/10.6084/m9.figshare.23717556>

Parent Article DOI: <https://doi.org/10.1364/BOE.494518>

# Mapping optical scattering properties to physical particle information in singly and multiply scattering samples: supplemental document

## 1. OCT SYSTEM CHARACTERIZATION

### A. Fourier optics simulations of beam behavior and $H(z)$

In order to apply a confocal function ( $H(z)$ ) correction to data that had been collected using a clipped or segmented incident beam, we performed Fourier optics calculations, similar to those described in Yin *et al.*, [1] to determine the shape of the resulting  $H(z)$  curve. The use of previously formulated methods [2] to remove the impact of  $H(z)$  from the overall OCT intensity signal rely on the ability of  $H(z)$  to be simplified based on approximations related to the incident beam having a Gaussian profile,[3] and are not necessarily applicable in situations where the incident beam cannot be described as Gaussian.

The field of a forward-propagating beam with Gaussian profile,  $E_+(x, z)$ , was modeled in 2-D, with the "+" indicating forward propagation. Masks were applied to this Gaussian profile to account for different beam clipping extents by the iris diaphragm or segmentation by the pathlength multiplexing element at the point of the free-space collimated beam. Fields were then propagated through air and focused by the  $10 \times$  objective lens (effective focal length = 18 mm) to yield the beam intensity maps ( $|E_+(x, z)|^2$ ) converging at the focus as shown in Figure A-1(a, b).

The back-propagating electric field was modeled as  $E_-(x, z) = E_+(x, z - \Delta z)$  where  $\Delta z$  accounts for the offset of the focal plane position. The confocal function effectively describes the power coupling efficiency,  $H$ , of the overlap integral of  $E_+(x, z)$  and  $E_-(x, z)$ . Using  $E_+(x, z)$  and  $E_-(x, z)$ , we calculated  $H(z)$  as [4]

$$H(z) = \frac{|\int E_+ E_- dx|^2}{\int |E_+|^2 dx \int |E_-|^2 dx}, \quad (S1)$$

where integral limits range from  $[-\infty, \infty]$ . In the case of a focused Gaussian beam, this expression simplifies to [3]

$$H(z) = \frac{1}{\left(\frac{z - z_f}{Z_R}\right)^2 + 1} \quad (S2)$$

where  $z_f$  and  $Z_R$  are beam focal plane location (e.g.,  $\Delta z$ ) and Rayleigh range, respectively.

In determined  $H(z)$  for each segmented beam case, we found that profiles were generally still able to be well-approximated by fitting to Eq. S2, affirming the validity of using strategies previously developed [2, 3] to account for the impact of the confocal function on the intensity decay of a singly-scattering sample (Fig. S1).

Our custom routine for mapping confocal function parameters used height-varying measurements similarly to methods proposed by Dwork *et al.* to derive spatially-varying  $Z_R$  and  $z_f$  under a given set of focusing conditions. For a given set of imaging experiments, the OCT system reference arm was kept at a constant position, thus the focal plane was also maintained at a constant depth in the tomogram. Based on the position of the calibration phantoms with respect to the objective lens, the optical depth of the focal plane shifted due to round-trip path length changes traversing different extents of the sample. However, given the constant position of the reference arm, we were able to compensate these optical path differences based on automated sample surface detection and axial distance adjustment by the phantom refractive index (1.34, equivalent to that of water) to verify the common position of the focal plane once these aspects were accounted for (Fig. S2). This made it possible to use this common  $z_f$  in confocal function compensation applied to all OCT intensity data, based on sample surface detection and refractive-index optical path adjustment to accurately determine the  $z_f$  position in each B-scan.

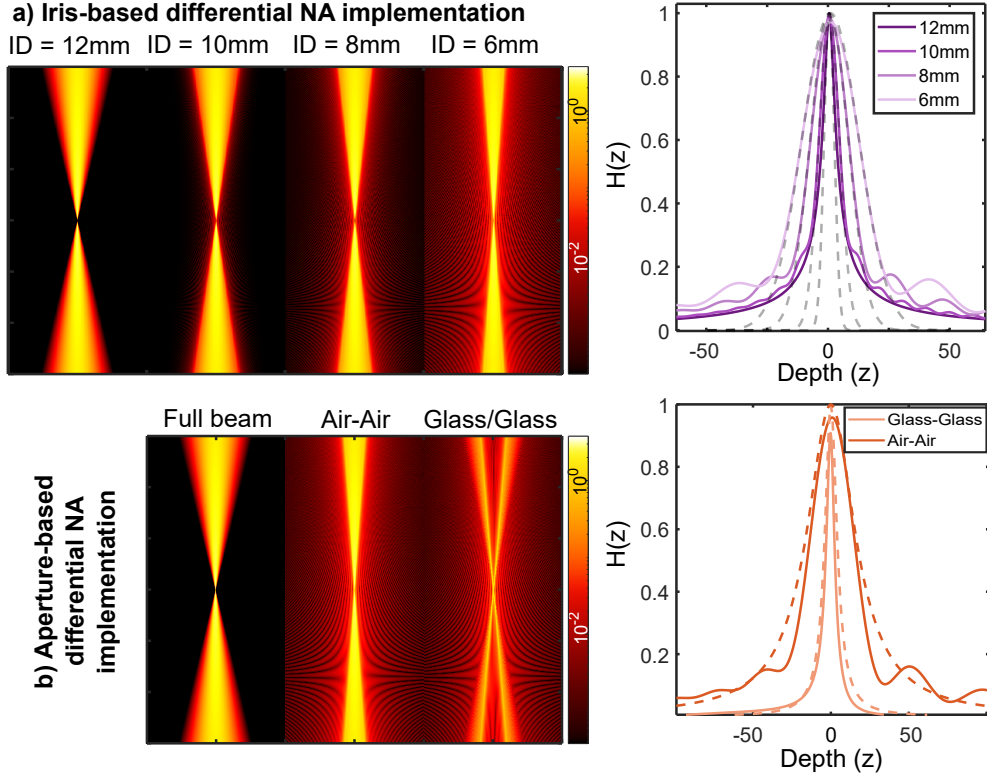


**Fig. S1.** Focused Gaussian beams under different clipping (a) and segmentation (b) schemes were modeled and used to find  $H(z)$  for each case. Dashed lines show fits to Eq. S2 for respective  $H(z)$  curves.

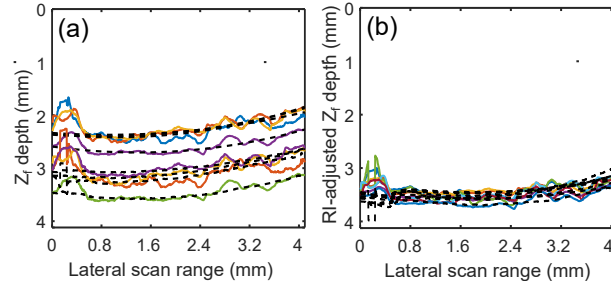


**Fig. S2.** Determining focal plane position in calibration phantoms. Variations in determined  $z_f$  due to variation in axial sample position (a) were compensated by accounting for sample surface position and refractive index to confirm constant focal plane position (b).

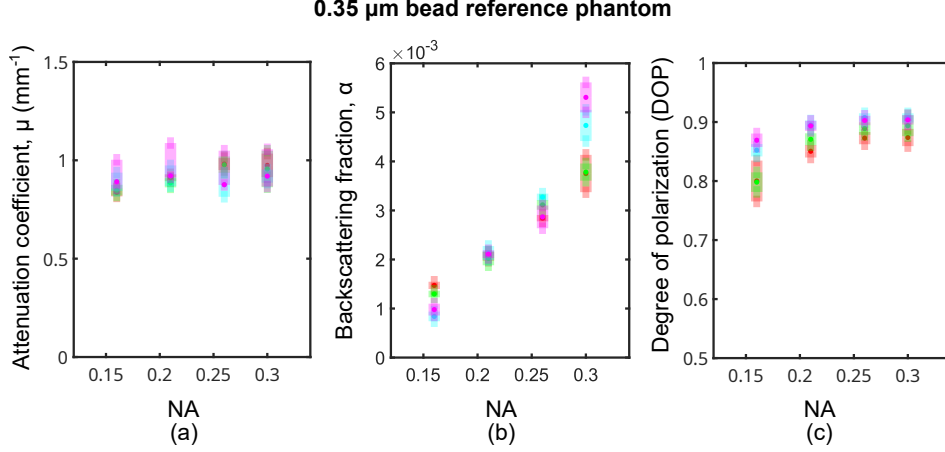


**Fig. S3.** In the 0.35  $\mu\text{m}$  reference calibration phantom, consistent  $\mu(z)$  (a) and DOP (c) were measured regardless of OCT system configuration, and  $\alpha$  values (b) increased linearly as expected with increasing NA. Data acquired at each focal plane position and system NA were averaged over  $n = 4$  measurements corresponding to the four different droplet phantom measurements acquired along with calibration data. Error bars represent standard deviation between these  $n = 4$  measurements.

## 2. PHANTOM IMAGING

As a form of methods validation and to determine the appropriate incident light intensity ( $L_0$ ) to use in calculating backscattering fractions under various differential NA conditions, scattering behavior was quantified for a region of the solid bottom phantom layer, made of 0.35  $\mu\text{m}$  beads embedded in agar, imaged to the right of the droplet ROI in each layered phantom dataset (see Fig. 2, main manuscript). In this phantom, which was presumed to be predominantly singly scattering due to small particle size ( $g = 0.23$ ),  $\mu(z)$  and DOP were found to be consistent throughout all datasets with variable system NA and focal plane position, and  $\alpha$  was found to increase linearly with NA as expected (Fig. S3). Some variation was observed due to inhomogeneities in sample structure, which complicated image processing steps using our layer-based scattering property calculation methods.

To quantify the relative impact of multiple scattering throughout phantoms of varying bead diameter at a high volume fraction ( $v_f = 0.012$ ), the average  $\mu_i(z)$  measured at a given  $i^{\text{th}}$  NA at each of the four focal plane positions was compared as a ratio to the average  $\mu_{low}(z)$  acquired at the lowest NA at each focal plane position [Fig. S5(a)]. As an alternative visualization, our proposed Multiple Scattering Index (MSI) computes relative changes with  $\mu(z)$  with NA as  $\mu_{low}(z)|\mu_i(z) - \mu_{low}(z)|$  [Fig. S5(b)]. Each metric indicated increasing impact of multiple scattering with progressively higher system NA, particularly at large (1.5  $\mu\text{m}$ , 3.0  $\mu\text{m}$ ) bead sizes.

## 3. TISSUE IMAGING

In addition to the relative nuclear density map provided in Figure 6 of the main manuscript, nuclei were also assessed more quantitatively throughout murine brain tissue. Using QuPath, the local diameters and NCR values (Fig. S6) were mapped to better understand the optically-derived scattering particle size and concentration information.

One source of uncertainty in our methods to obtain physical particle information from optical properties is the estimation of the refractive indices of particles,  $n_{part}$ , and their surrounding medium. Using estimates of nuclei refractive indices we found in existing literature[5–7] and a medium refractive index of water (1.34), we examined how varying  $n_{part}$  resulted in alteration to output particle sizes and concentrations (Fig. S7). In general, alterations to refractive index resulted in global changes in  $d$  and  $v_f$ , but maintained overall trends in the ways these physical properties varied between different tissue areas.

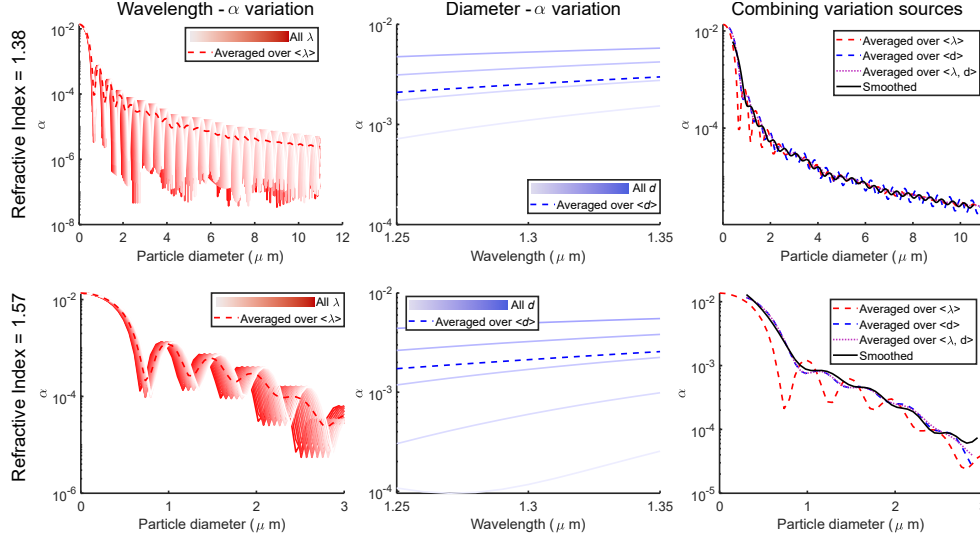


**Fig. S4.** Variation in  $\alpha$  is shown with respect to wavelength ( $\lambda$ ) over the full swept source bandwidth (1.25 – 1.35  $\mu\text{m}$ ) at a range of scattering particle diameters ( $d$ ), as well as the  $\lambda$ -averaged profile with respect to  $d$  (left column). Variation in  $\alpha$  is also shown for a 0.5  $\mu\text{m}$  bead sample over  $d$  within manufacturer-specified coefficient of variation, ranging from [0.45, 0.55]  $\mu\text{m}$ , at a range of  $\lambda$ , as well as the  $d$ -averaged profile with respect to  $\lambda$  (middle column). In the right column, the curves averaged over  $d$  and  $\lambda$  from the left and middle panels are plotted against their jointly averaged result, as well as the filtering-based smoothed  $\alpha$  functions used for these experiments. Results in the top row are shown for a particle refractive index of 1.38 and in the bottom for a refractive index of 1.57 to represent both the tissue and phantom experiments, respectively.

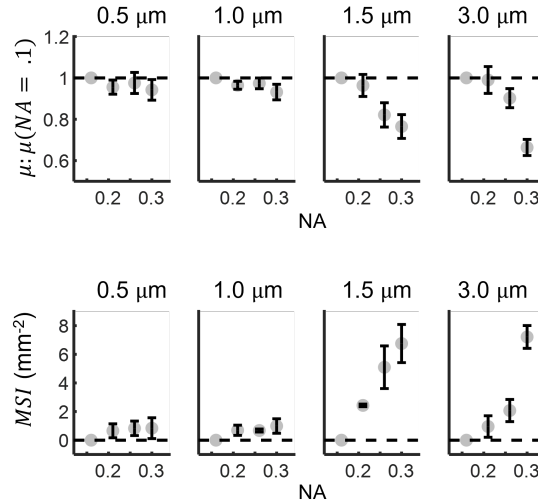


**Fig. S5.** Comparing impact of system NA on  $\mu(z)$  measurements.  $\mu$  measured at each NA, averaged across all focal plane positions, were compared directly as a ratio to the  $\mu$  measured at the lowest system NA used (a), as well as using our formula for Multiple Scattering Index (b).

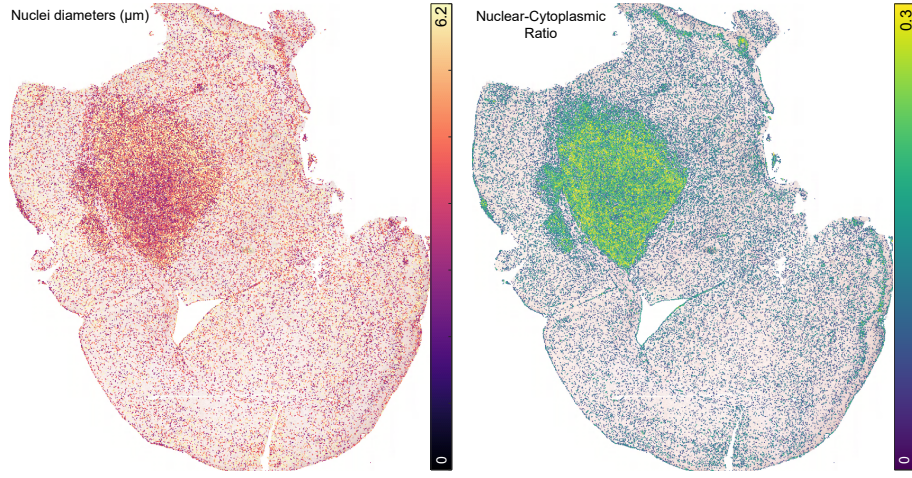


**Fig. S6.** Murine tissue histology was analyzed in QuPath to calculate the regional variation in nuclei diameters and nuclear-cytoplasmic ratio (NCR) throughout the healthy cerebellum and tumor-bearing region. The tumor bearing region was found to have higher NCR than the surrounding healthy cerebellar tissue, and moderate to large nuclei diameters.

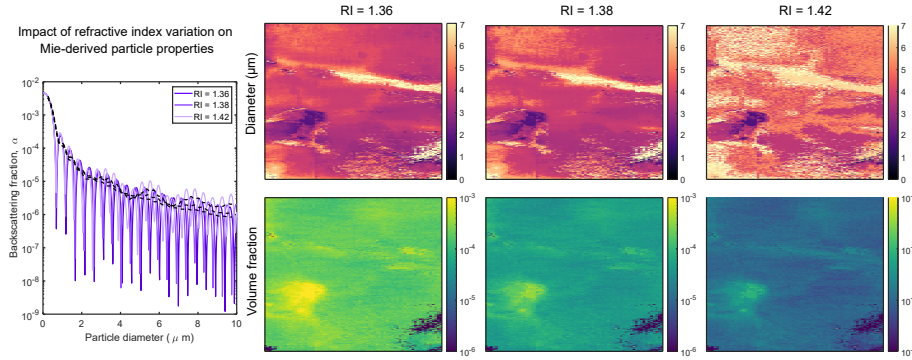


**Fig. S7.** Three refractive index values (1.36, 1.38, 1.42) varying over ranges for previously reported for cell nuclei were used to calculate particle  $\alpha$ -diameter curves, which were smoothed and used to calculate optically-derived particle diameters ( $d$ , top row) and volume fractions ( $v_f$ , bottom row) based on each input refractive index value.

## REFERENCES

1. B. Yin, J. Dwelle, B. Wang, T. Wang, M. D. Feldman, H. G. Rylander, and T. E. Milner, "Fourier optics analysis of phase-mask-based path-length-multiplexed optical coherence tomography," *J. Opt. Soc. Am. A*, JOSAA **32**, 2169–2177 (2015).
2. N. Dwork, G. T. Smith, J. M. Pauly, and A. K. Ellerbee Bowden, "Automated Estimation of OCT Confocal Function Parameters from two B-Scans," in *Conference on Lasers and Electro-Optics*, (OSA, San Jose, California, 2016), p. AW1O.4.
3. T. van Leeuwen, D. Faber, and M. Aalders, "Measurement of the axial point spread function in scattering media using single-mode fiber-based optical coherence tomography," *IEEE J. Sel. Top. Quantum Electron.* **9**, 227–233 (2003).
4. R. E. Wagner and W. J. Tomlinson, "Coupling efficiency of optics in single-mode fiber components," *Appl. optics* **21** (1982).
5. M. Schürmann, J. Scholze, P. Müller, J. Guck, and C. J. Chan, "Cell nuclei have lower refractive index and mass density than cytoplasm," *J. Biophoton* **9**, 1068–1076 (2016).
6. H. Zhang, Z. A. Steelman, D. S. Ho, K. K. Chu, and A. Wax, "Angular range, sampling and noise considerations for inverse light scattering analysis of nuclear morphology," *J. Biophotonics* **12**, e201800258 (2019).
7. W. Choi, C. Fang-Yen, K. Badizadegan, S. Oh, N. Lue, R. R. Dasari, and M. S. Feld, "Tomographic phase microscopy," *Nat Methods* **4**, 717–719 (2007).